


Measurement of residual cross sections in the ${}^7\text{Li} + {}^{89}\text{Y}$ reaction up to 5.7 MeV/nucleon and analysis of fusion mechanisms

Rinku Prajapat  and Moumita Maiti **Department of Physics, Indian Institute of Technology Roorkee, Roorkee-247667, Uttarakhand, India*
 (Received 8 October 2019; revised manuscript received 23 December 2019; accepted 24 January 2020; published 18 February 2020)

Different modes of fusion phenomena observed in the isolated experiments are not yet fully understood. To comprehend these fusion mechanisms, more experimental studies are necessary. In view of this, a new measurement of residual cross sections from the ${}^7\text{Li}$ -induced reaction on ${}^{89}\text{Y}$ has been reported in this article within the 2.7–5.7 MeV/nucleon energy range. The γ -ray spectrometry has been used to identify the residues ${}^{93m}\text{Mo}$, ${}^{92m}\text{Nb}$, ${}^{89}\text{Zr}$, ${}^{91m}\text{Y}$, and ${}^{90m}\text{Y}$ produced in the reaction. A systematic analysis of the complete and incomplete fusion dynamics has been carried out by comparing the measured excitation functions with the equilibrium and pre-equilibrium reaction models in the framework of EMPIRE3.2.2 and ALICE19. A strong indication of the occurrence of incomplete fusion has been realized within the energy range considered; hence the incomplete fusion strength is discussed in detail. The product yield of ${}^{93m}\text{Mo}$, which is a candidate radionuclide for radiopharmaceuticals, has been estimated.

DOI: [10.1103/PhysRevC.101.024608](https://doi.org/10.1103/PhysRevC.101.024608)

I. INTRODUCTION

A collision between two heavy nuclei may lead to a variety of nuclear reaction processes such as deep-inelastic scattering, quasifission, equilibrium (EQ), pre-equilibrium (PEQ), etc. depending on the projectile energy and structural properties of the interacting partners. Although the interaction of nuclei is commonly classified in two categories: elastic scattering and reaction, which includes mainly inelastic scattering, transfer, and fusion, it is essential to have a thorough understanding of the heavy-ion fusion dynamics resulting from the more complex energy and momentum sharing process between the two colliding nuclei around and above the Coulomb barrier.

In the case of tightly bound heavy projectiles, a significant enhancement in the fusion cross section was observed in the subbarrier region compared with the one-dimensional barrier penetration model (1D-BPM). The reason for enhanced fusion cross section was understood in terms of the internal degrees of freedom of the colliding nuclei such as couplings of the collective states of interacting partners and nucleon transfer, deformation, vibration, etc. [1–5]. However, the fusion mechanisms of weakly bound stable (${}^6\text{Li}$ and ${}^9\text{Be}$) and unstable halo (${}^{11}\text{Li}$, ${}^{7,11}\text{Be}$, and ${}^8\text{B}$) nuclei are quite multifarious. Thus, processes like complete and incomplete fusion (CF-ICF), elastic breakup (EBU), transfer followed by a breakup, appear in the reaction dynamics. Full amalgamation of the projectile (without breakup) with the target leads to the formation of the compound nucleus (CN), which is termed as direct complete fusion (DCF); if all the chunks of the projectile (after the breakup) fuse with the target, the process is known

as sequential complete fusion (SCF). However, measurement of residues could hardly describe the occurrence of DCF and SCF since both the methods leading to the formation of the same CN. Likewise, if one of the chunks fuses with the target and others fly away, the process is called as ICF; if the target captures none of the fragments, the mechanism is called EBU.

The contribution of ICF over CF for the cluster-structured nuclei (${}^6,{}^7\text{Li}$, ${}^9\text{Be}$, ${}^{12,13}\text{C}$, ${}^{16}\text{O}$, and ${}^{19}\text{F}$) and dependency of ICF strength fraction F_{ICF} on different entrance channel parameters have been studied over the past few years within the ≈ 3 –10 MeV/nucleon energy range [6–11]. It has been reported that F_{ICF} increases linearly with $Z_P Z_T$ [11] and target charge Z_T [12] contrary to that has been observed independent of target charge Z_T in Ref. [13]. Recently, Chauhan *et al.* [14] measured the production cross sections of the residues from the ${}^7\text{Li} + {}^{\text{nat}}\text{Ta}$ reaction up to 6.5 MeV/nucleon and described the possibility of occurrence of ICF or transfer of one nucleon followed by ICF in the α -emitting channels. However, beyond the critical energy of ≈ 15 MeV/nucleon, none of the breakup fragments fuse in the peripheral collisions, and the probability of occurrence of the ICF process gets reduced [15]. In central collisions such as CF, a projectile transfers its total angular momentum to the target within the limit of $0 < l \leq l_{\text{crit}}$, while in peripheral collisions and the ICF process, partial angular-momentum transfer occurs with $l \geq l_{\text{crit}}$. For the latter case, the potential pocket vanishes, and it restricts the fusion of colliding nuclei until a fragment of the projectile becomes free (P^i : spectator) to release viable angular momentum. After its emission, the remnant fragment (P^j : participant) moves with the remnant angular momentum ($\leq l_{\text{crit}}^{i+T}$) [15,16].

The enhancement of the CF cross section at the subbarrier energies, hindrance in the deep subbarrier, and suppression in the above-barrier region have also been reported for the

*moumita.maiti@ph.iit.ac.in; moumifph@gmail.com

weakly bound stable projectiles [17,18]. In the existing literature, no suppression in the fusion cross section was noticed for the weakly and tightly bound projectile-induced reactions on the light and medium-light mass targets [19,20], while $\approx 20\%$ – 35% suppression in the fusion cross section was observed for the weakly bound projectile-induced reaction in the medium and light heavy-mass targets like ${}^6\text{Li} + {}^{90,96}\text{Zr}$, ${}^{144}\text{Sm}$, ${}^7\text{Li} + {}^{144,154}\text{Sm}$, ${}^{159}\text{Tb}$ and ${}^9\text{Be} + {}^{89}\text{Y}$, ${}^{144}\text{Sm}$ as compared with the coupled-channel (CC) calculations without considering breakup and transfer couplings [21–27]. However, for the reactions with heavy-mass targets, ${}^6,7\text{Li} + {}^{209}\text{Bi}$ and ${}^9\text{Be} + {}^{208}\text{Pb}$, $\approx 30\%$ – 40% suppression in CF has been reported [28]. Nucleon transfer followed by breakup has been observed for the ${}^7\text{Li}$ projectile: breakup into $\alpha + \alpha$ after a proton pickup from the target and that into $\alpha + d$ after a neutron stripping from the projectile to the target; however, the $\alpha + \alpha$ channel is less probable as compared with $\alpha + d$ and $\alpha + t$ (direct breakup) [29,30]. It was shown that breakup of ${}^7\text{Li}$ into $\alpha + d$ is more favored compared with $\alpha + t$ channel in ${}^7\text{Li} + {}^{65}\text{Cu}$ reaction [31]. Gull *et al.* [32] reported ICF analysis in the α -emitting channels using recoil-range distribution and observed that ICF strength fraction increases with Z_T . Our group has also investigated the CF-ICF reactions for ${}^7\text{Li} + {}^{\text{nat}}\text{Mo}$, ${}^7\text{Li} + {}^{93}\text{Nb}$, and ${}^7\text{Li} + {}^{\text{nat}}\text{Ta}$ systems within the 3.5–7 MeV/nucleon energy range [6,9,14], reported the study of EQ and PEQ reaction processes in ${}^7\text{Li}$ -, ${}^9\text{Be}$ -, ${}^{11}\text{B}$ -, and ${}^{12}\text{C}$ -induced reactions on the medium-mass targets which could produce some medically relevant radionuclides such as ${}^{97}\text{Ru}$ (2.83 d), ${}^{101m}\text{Rh}$ (4.34 d), and ${}^{207-210}\text{At}$ (1.63–8.1 h) [33–45]. The contribution of PEQ emissions was observed in the high-energy tail of the excitation function, particularly in the $3n$ channel [33,34,46].

In view of the discrepancies observed in the weakly bound projectile mediated reactions, more experimental data are required to understand the phenomena, especially in the light-medium and medium-mass targets. This article describes a detailed study of the fusion mechanism, contribution of CF and ICF processes, and ICF strength fraction for ${}^7\text{Li} + {}^{89}\text{Y}$ systems within 19–40 MeV energy range. Experimental details of this work have been presented in Sec. II, the description of model calculations has been provided in Sec. III. Section IV sheds light on the analysis of measured data, and finally, Sec. V concludes the report.

II. EXPERIMENTAL DETAILS

The experiment was performed at the 14UD BARC-TIFR Pelletron facility, Mumbai, India. Self-supporting thin foils of pure (99.99%) natural ${}^{89}\text{Y}$ and ${}^{27}\text{Al}$ were prepared by proper rolling. The thickness of Y and Al foils were ≈ 2 – 3.9 mg/cm² and ≈ 1.5 – 3.0 mg/cm², respectively. Each stack of targets was assembled by using two or three foils of Y, the Al catcher foils were placed behind each target foil to catch the recoiled residues in the forward beam direction and also for the beam energy degradation so that suitable energy separation between successive target foils could be accomplished. Each stack of targets was bombarded by the ${}^7\text{Li}$ beam; the beam energies were in the range 19–40 MeV in the laboratory frame of reference. The average beam flux

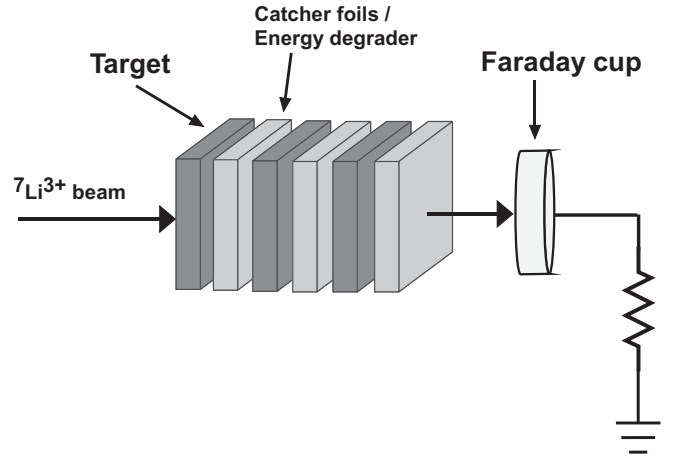


FIG. 1. Schematic diagram of target-catcher foil arrangement that was used in the experiment.

(${}^7\text{Li}^{3+}$) was $\approx 7 \times 10^{10}$ particles/s during the experiment. The beam current was maintained almost constant, and the average charge of ≈ 456 μC was collected for each set of irradiation. The total charge was measured by an electron-suppressed Faraday cup installed behind the target stack. The schematic setup of the stack-foil arrangement has been shown in Fig. 1. The energy degradation of the incident beam in each foil of a stack has been predicted using the Monte Carlo-simulation based SRIM (the stopping and range of the ions in the matter) code [47]. The projectile energy at a particular target is the average of the incident and outgoing energy.

After the end of bombardment (EOB), the populated residues in each target (${}^{89}\text{Y}$) foil were identified following their characteristics γ rays and decay profile with the help of γ -ray spectrometry. The large-volume high-purity germanium detector used in this study was precalibrated using the conventional sources ${}^{137}\text{Cs}$ (30.08 y), ${}^{152}\text{Eu}$ (13.517 y), and ${}^{60}\text{Co}$ (5.27 y) of known activity. The energy resolution of the detector was 2.0 at 1332 keV γ rays of ${}^{60}\text{Co}$. The spectroscopic properties of the residues are tabulated in Table I. The unique characteristic γ rays have been used to measure the cross section of the i th residue at the energy E using the following activation relation:

$$\sigma_i(E) = \frac{\lambda_i N_i(t) e^{\lambda_i t_w}}{\xi_\gamma \theta_\gamma \rho_{t_g} \phi (1 - e^{-\lambda_i t_r})(1 - e^{-\lambda_i t_c})}, \quad (1)$$

where λ_i is the decay constant, $N_i(t)$ is the area counts under the photopeak, geometry-dependent efficiency of the detector is ξ_γ , branching ratio of characteristic γ ray is θ_γ , ρ_{t_g} is the areal density of target nuclei, incident beam flux is ϕ . The counting time, irradiation time, and the waiting time between the EOB and measurement are denoted by t_c , t_r , and t_w , respectively.

The sources of uncertainty in the cross section measurement are the following:

- (1) Maximum inaccuracy in the target thickness measurement was estimated as $\approx 2\%$.
- (2) Uncertainty in the measurement of geometry dependent efficiency of the detector was $\leq 2\%$.

TABLE I. Nuclear spectroscopic data [61] of the populated residues in ${}^7\text{Li} + {}^{89}\text{Y}$ reaction.

Residue	J^π	$T_{1/2}$	Decay mode (%)	E_γ (keV)	I_γ (%)
${}^{93m}\text{Mo}$	$21/2^+$	6.85 h	IT ^a (99.88),	263.05	57.4
			$\epsilon^b + \beta^+$ (0.12)	684.69	99.9
				1477.14	99.1
${}^{92m}\text{Nb}$	2^+	10.15 d	$\epsilon + \beta^+$ (100)	934.44	99.15
${}^{89}\text{Zr}$	$9/2^+$	78.41 h	$\epsilon + \beta^+$ (100)	909.15	99.04
${}^{91m}\text{Y}$	$9/2^+$	49.71 min	IT (100), $\beta^- < (1.5)$	555.57	95.0
${}^{90m}\text{Y}$	7^+	3.19 h	IT (100), $\beta^- (1.8 \times 10^{-3})$	202.53	97.3
				479.51	90.74

^aIsomeric transition.

^bElectron capture.

- (3) Due to the fluctuation in beam current, error in the incident beam flux was considered to be $\approx 6\%$ – 7% .
- (4) Dead time of the detector was kept $\leq 10\%$ by adjusting the geometry of measurement. Statistical error in the background-subtracted peak area count, which was varying for each residue at different projectile energies, has been considered in the error calculation.
- (5) There may be a finite error in the estimation of beam energy due to the degradation of energy in the successive target-catcher foils. However, energy straggling is expected to be small [48,49].

Total error corresponding to each cross section has been estimated considering all those factors, and the measured data are reported in this article up to 95% confidence level. The uncertainty associated with the estimation of the incident projectile energies includes the error in the SRIM calculation and the determination of target thickness.

III. MODEL CALCULATION

The reaction model code ALICE19 [50] is based on the EQ and PEQ reaction processes, however, it adopted Weisskopf-Ewing (WE) formulation for EQ, Monte Carlo formulation of hybrid- or geometry-dependent hybrid model (HMS) for PEQ reaction [50], and Bohr-Wheeler approach for fission modes. The code is applicable for light as well as heavy incident particles. In the framework of this code, one could select different level densities such as Fermi gas (FG) with back-shifted pairing, Kataria-Ramamurthy (KR), Obninsk, and Gilbert-Cameron model (GCM). Therefore, we consider the s -wave approximation and three nuclear level densities such as FG, KR, and GCM in the present calculation within the framework of ALICE19. Since KR and GCM are invariant with respect to the level-density parameter, we consider the effect of the level-density parameter $a = A/K$ in the FG model, where A is the mass number of the compound nucleus, and K is an adjustable parameter; the value of K is 9, 10, and 11 in our calculation. At each stage of the deexcitation, the angular distribution of emitted particles, which are mostly from the PEQ process, is calculated by the Chadwick-Oblozinsky linear momentum conservation model. ALICE19 considers the classical sharp cutoff algorithm as well as the nuclear optical

model for the estimation of inverse reaction cross sections. Binding energies and Q values of the spallation nuclide, n , p , and α are calculated internally from the Myers-Swiatecki mass formula (Lysekil).

The nuclear reaction model code EMPIRE3.2.2 [51] has been used for the estimation of cross sections of the residues from the ${}^7\text{Li} + {}^{89}\text{Y}$ reaction to interpret the measured data. EMPIRE considers three significant types of reactions of heavy projectiles: direct reactions, PEQ, and EQ or CN reactions in its framework. The direct reactions are estimated by the coupled-channel (CC) approach and distorted-wave Born approximation (DWBA). The CC method is useful to study the elastic-scattering channels and low-lying states, which are strongly excited in inelastic scattering for deformed nuclides. Whereas the DWBA is valid for small deformation and is commonly used for inelastic scattering, for both strongly and weakly coupled levels, the simplified coupled-channel approach (CCFUS) [52] is used for heavy-ion fusion. EMPIRE uses quantum-mechanical and phenomenological models for PEQ processes. The quantum-mechanical PEQ models are based on the multistep direct (MSD) and multistep compound (MSC) theories, while phenomenological models are the exciton model (EM) and the Monte Carlo pre-equilibrium code. However, the understanding of PEQ reactions for the heavy ions is not yet evident in the quantum-mechanical models; hence, they are not popularly used. The EM has been used to calculate PEQ emissions in the present calculation, and the Hauser-Feshbach (HF) formalism has been used to estimate the EQ cross sections of the residues with width fluctuation correction, necessary to establish a correlation between the incident and exit channels. To investigate the effect of nuclear level-density models in the residual cross sections, three phenomenological level-density models: the Gilbert-Cameron Model (GCM) [53], the generalized superfluid model (GSM) [54], and the enhanced generalized superfluid Model (EGSM) [55], have been used. In all the level-density models, EMPIRE considers the collective (rotational or vibrational) excitations, which enhanced the theoretical cross sections.

IV. DATA ANALYSIS AND DISCUSSIONS

The ${}^7\text{Li}$ -induced reactions in ${}^{89}\text{Y}$ led to the formation of ${}^{93m}\text{Mo}$, ${}^{92m}\text{Nb}$, ${}^{89}\text{Zr}$, ${}^{91m}\text{Y}$, and ${}^{90m}\text{Y}$ radionuclides within

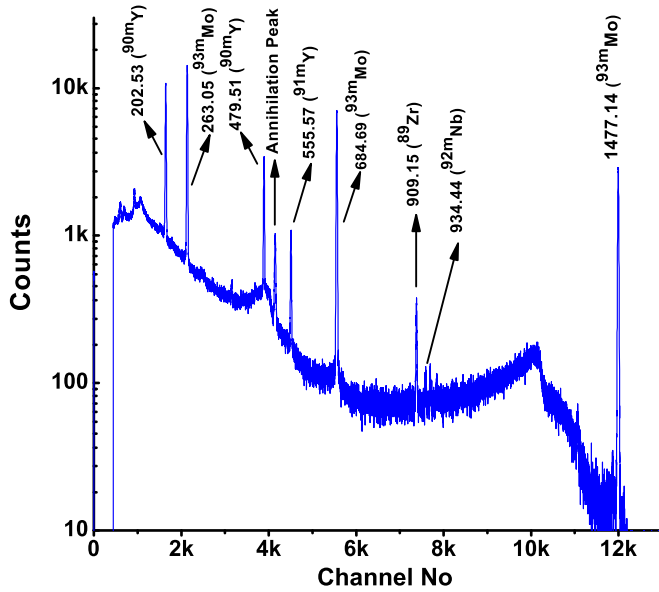


FIG. 2. Typical γ -ray spectrum of the 39.4 MeV ${}^7\text{Li}$ -irradiated ${}^{89}\text{Y}$ collected 49 min after EOB. The energy of the γ -ray peaks is in keV.

19–40 MeV incident energy. The residues were identified from their characteristic γ rays and decay profile. A typical γ -ray spectrum of the ${}^7\text{Li}$ -irradiated ${}^{89}\text{Y}$ target at 39.4 MeV incident energy, collected after 49 min of the EOB, is shown in Fig. 2 where residues are indicated corresponding to their characteristic γ peaks. The dead-time corrected peak area (background subtracted) of all the unique γ rays of each residue was analyzed to measure the activity, and the cross sections of the residues were calculated from Eq. (1). Experimentally measured cross sections, tabulated in Table II, are compared with the theory as presented in Figs. 3–5. The CF and ICF cross sections, along with the variation of ICF strength fraction F_{ICF} , are portrayed in Figs. 6 and 7 with respect to the incident energy. The experimental data are shown by symbols with uncertainty, while lines present the theoretical predictions.

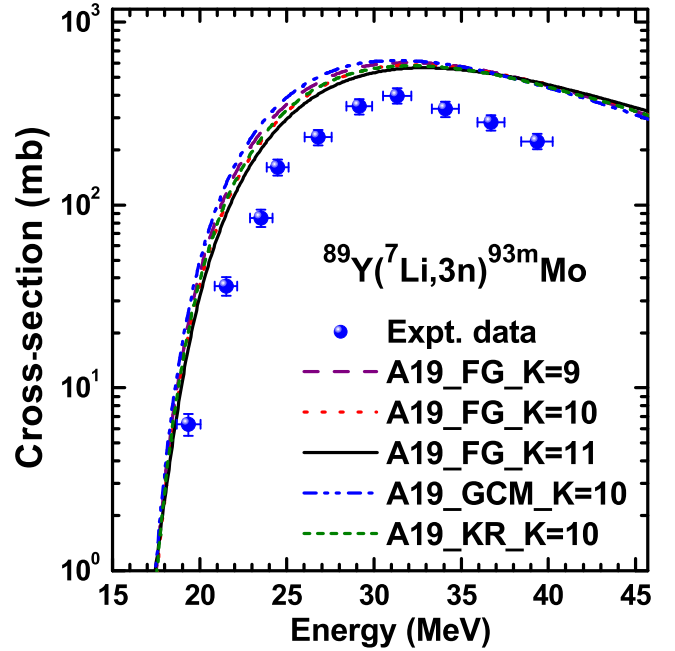


FIG. 3. Comparison of measured cross sections of ${}^{93m}\text{Mo}$ with theoretical predictions from ALICE19 (denoted A19) with KR, GCM, and FG (with $a = A/K$, $K = 9, 10, 11$) level-density models.

A. Residual cross sections

The measured cross sections of ${}^{93m}\text{Mo}$ are compared with the theoretical cross sections estimated from ALICE and EMPIRE, as presented in Figs. 3 and 4(a).

It is evident from Fig. 3 that the trend of the measured cross sections of ${}^{93m}\text{Mo}$ is well reproduced by the excitation functions obtained from ALICE, which uses the WE and HMS models with FG, GCM, and KR level density. The effect in residual cross sections has also been studied by varying the level-density parameter ($a = A/K$, $K = 9, 10$, and 11) within the framework of the FG model. Note that two other models, KR and GCM, stay invariant under the change of level-density parameter; hence $K = 10$ has been used for those calculations. It could be noticed that all the level-density models show a similar trend throughout the energy range. Although all the

TABLE II. Cross section of residues at various incident energies.

Energy (MeV)	Cross section (mb)					$\sum \sigma_{\text{res}}$
	${}^{93m}\text{Mo}$	${}^{92m}\text{Nb}$	${}^{89}\text{Zr}$	${}^{91m}\text{Y}$	${}^{90m}\text{Y}$	
19.4 ± 0.7	6.3 ± 0.9			2.0 ± 0.3	0.7 ± 0.1	9.0 ± 0.9
21.5 ± 0.7	36.2 ± 4.2			3.8 ± 0.5	1.5 ± 0.2	41.5 ± 4.2
23.5 ± 0.6	85.2 ± 9.1			5.2 ± 0.6	2.8 ± 0.4	93.2 ± 9.1
24.5 ± 0.6	161.4 ± 16.4	15.6 ± 3.4		6.3 ± 1.8	4.4 ± 0.6	187.7 ± 16.8
26.8 ± 0.8	235.4 ± 23.1	18.7 ± 3.2		10.4 ± 2.3	6.9 ± 0.9	271.4 ± 23.4
29.1 ± 0.7	346.7 ± 33.6	22.4 ± 3.8		11.4 ± 2.2	11.6 ± 1.4	392.1 ± 33.9
31.3 ± 0.8	396.8 ± 38.6	23.9 ± 3.8	3.2 ± 0.6	12.4 ± 1.4	18.8 ± 2.3	455.1 ± 38.8
34.1 ± 0.8	335.6 ± 32.7	29.5 ± 4.4	14.3 ± 2.0	13.5 ± 1.5	22.5 ± 2.5	415.4 ± 33.2
36.7 ± 0.8	283.3 ± 27.7	33.3 ± 4.9	44.6 ± 5.9	13.0 ± 1.4	28.3 ± 3.0	402.5 ± 28.9
39.4 ± 0.9	223.3 ± 21.8	52.8 ± 8.7	111.1 ± 12.1	14.6 ± 1.5	37.9 ± 3.9	439.7 ± 26.7

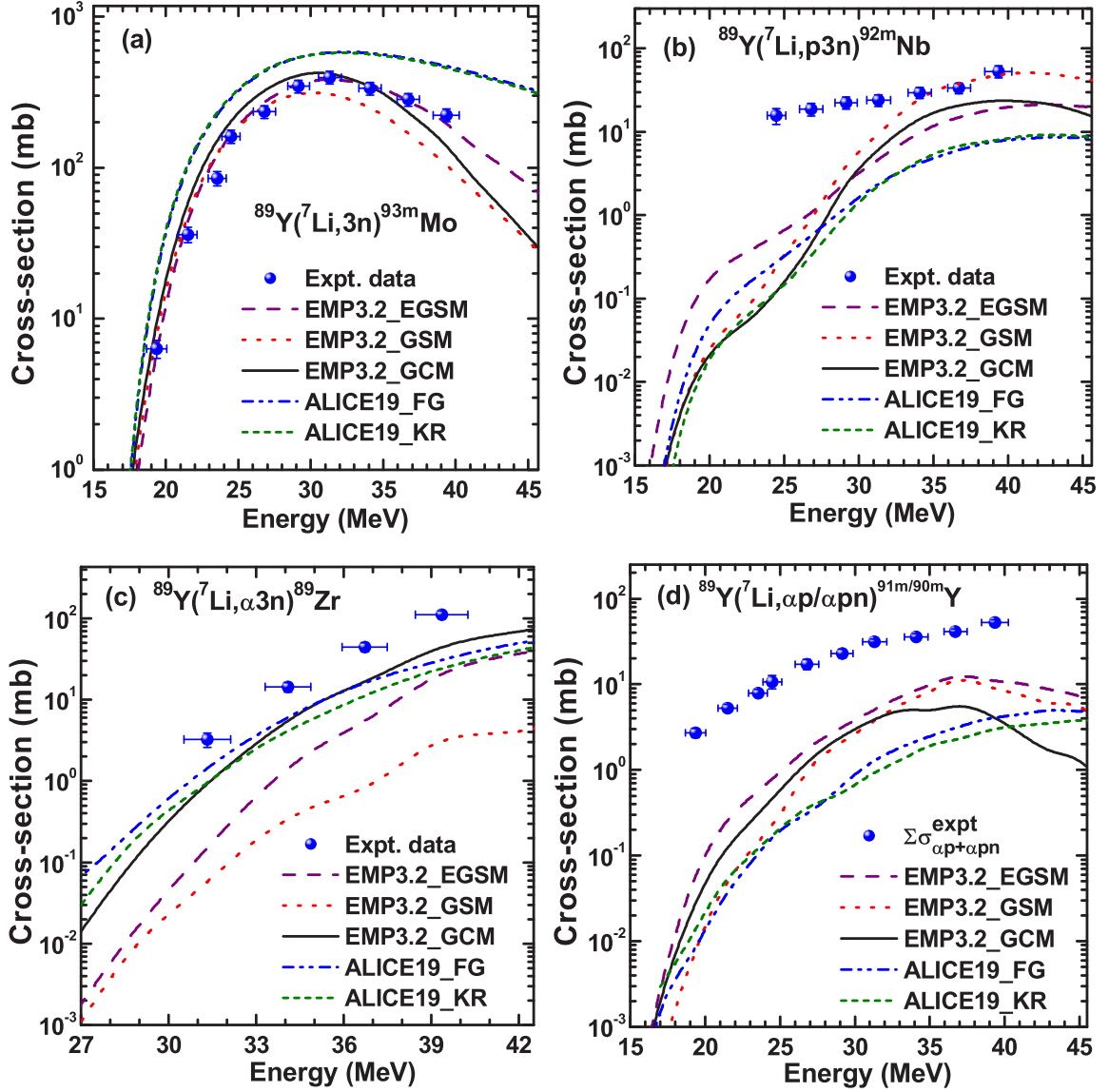


FIG. 4. Comparison between measured excitation function of (a) ^{93m}Mo , (b) ^{92m}Nb , (c) ^{89}Zr , and (d) sum of ^{90m}Y and ^{91m}Y with the theoretical predictions of EMPIRE3.2.2 (denoted by EMP3.2) and ALICE19.

excitation functions are close to each other, the absolute cross sections differ within $\approx 18\text{--}35$ MeV whereas, beyond 35 MeV, the cross sections are approximately equal. Among others, FG with $K = 11$ is close to the experimental data < 35 MeV, but it starts deviating beyond it. Altogether, the relative difference between the KR, GCM, and FG (with $K = 11$) is $\approx 3\%\text{--}25\%$ in the lower-energy range while it is $\leq 5\%$ in the higher-energy range. Critical observation shows that the FG level density with $a = A/10$ and the KR level density offer the best result in this case, and they are very close to each other. Therefore, the ALICE calculation with KR and FG with $a = A/10$ has been used for further analysis.

In general, it may be observed in Fig. 4 that ALICE and EMPIRE reproduce a similar shape of the excitation functions throughout the energy range. It is evident from Fig. 4(a) that the shape of the experimental excitation function is satisfactorily reproduced by the EMPIRE estimations, which have

used HF and EM with three different level-density models: EGSM, GSM, and GCM, throughout the energy range. On the other hand, ALICE with FG and KR level density shows the same trend of excitation function, but it overpredicts the data throughout the energy range. On the other hand, EMPIRE level densities are very close to each other and reproduce well the experimental cross sections up to ≈ 25 MeV, beyond which they start diverging. However, the EGSM estimation reproduces the data more accurately throughout the whole energy range while GSM and GCM are found to be $\approx 10\%\text{--}20\%$ less than the measured data beyond ≈ 30 MeV. Thus the production of ^{93m}Mo in the $3n$ channel in our observation has resulted from the PEQ and EQ neutrons. A similar trend of the cross sections was observed for the residues produced through the $3n$ channel in various heavy-ion-induced reactions [33,34,46]. It is established that PEQ nucleons have slightly higher energy compared with the emission of fully equilibrated nucleons.

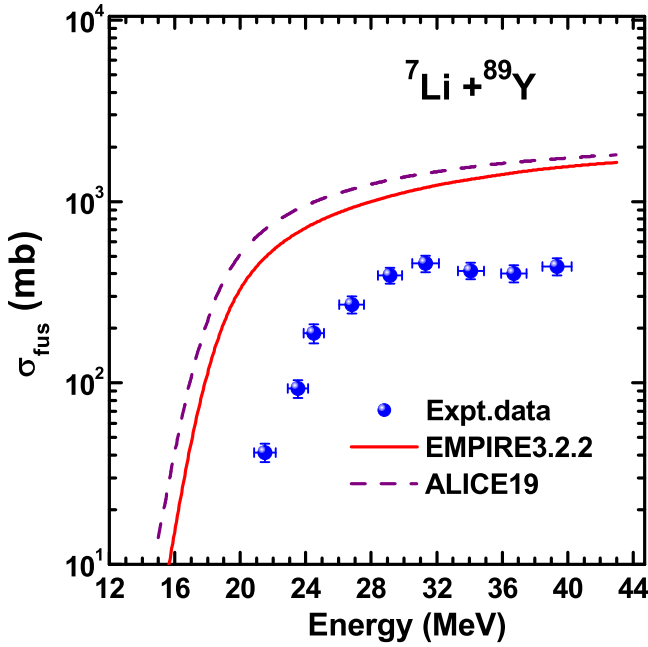


FIG. 5. Comparison of total fusion cross sections σ_{fus} as a function of energy E_{lab} with EMPIRE3.2.2 and ALICE19.

Thus, mixing of PEQ with EQ processes is necessary for the best reproduction of the experimental data.

The residues ^{92m}Nb and ^{89}Zr , which are expected from the $^7\text{Li}(^{89}\text{Y}, p3n)^{92m}\text{Nb}$ and $^7\text{Li}(^{89}\text{Y}, \alpha 3n)^{89}\text{Zr}$ reactions, have enhanced cross sections as compared with EMPIRE and ALICE, except for ^{92m}Nb where EMPIRE with GSM describes the data points beyond 34 MeV energy, as contemplated in Figs. 4(b) and 4(c), respectively. To evaluate if the α -emitting channels are produced via CF, a sum of the measured cross sections of ^{91m}Y and ^{90m}Y , whose productions are commonly assumed through the αp and αpn channels, have been compared with

the theoretical model calculations using the same set of input parameters that are used for the reproduction of $3n$ channel, as shown in Fig. 4(d). It is worth mentioning that the measured cross sections are significantly large compared with EMPIRE and ALICE, both of which consider the complete fusion of ^7Li in ^{89}Y in its calculation kernel. Thus, the observed enhancement in cross sections may be attributed to the ICF process.

The measured total fusion cross section, which is the sum of cross sections of the residues at a particular energy, has been compared with the predicted one from EMPIRE and ALICE in Fig. 5 over the energy range considered. The relative difference between the fusion cross sections of EMPIRE and ALICE is $\approx 18\%$, and the reason is possibly due to the adoption of two models for it; EMPIRE uses a simplified coupled-channel approach (CCFUS), and ALICE relies on the parabolic optical model to estimate the fusion cross section. The present measurement produces only $\approx 38\%$ of the total cross section estimated by EMPIRE, because the measured residual cross sections are analyzed mainly by using the EMPIRE platform. The observed difference, as seen in Fig. 5, between the measured and predicted values might be due to the following reasons: (i) in the breakup of ^7Li , some of the incident flux gets lost before the interaction, and this breakup effect is not included in theoretical calculations; (ii) short half-lives of the residues or some of the stable residues, which are populated through the xn , pxn , and αxn channels could not be measured by the present method.

Due to the low breakup threshold of the weakly bound and cluster-structured ^7Li projectile, it breaks up in the nuclear force field, and it has been confirmed by many on-line experiments that could observe the transfer channels such as (^7Li , ^6Li), (^7Li , ^5Li), (^7Li , ^8Be), (^7Li , ^6He), (^7Li , ^5He) followed by breakup into $\alpha + d$, $\alpha + p$, $\alpha + \alpha$, $\alpha + 2n$, and $\alpha + n$, respectively [56–58], and the direct breakup of ^7Li into $\alpha + t$ [30,58]. Hence the large production cross section

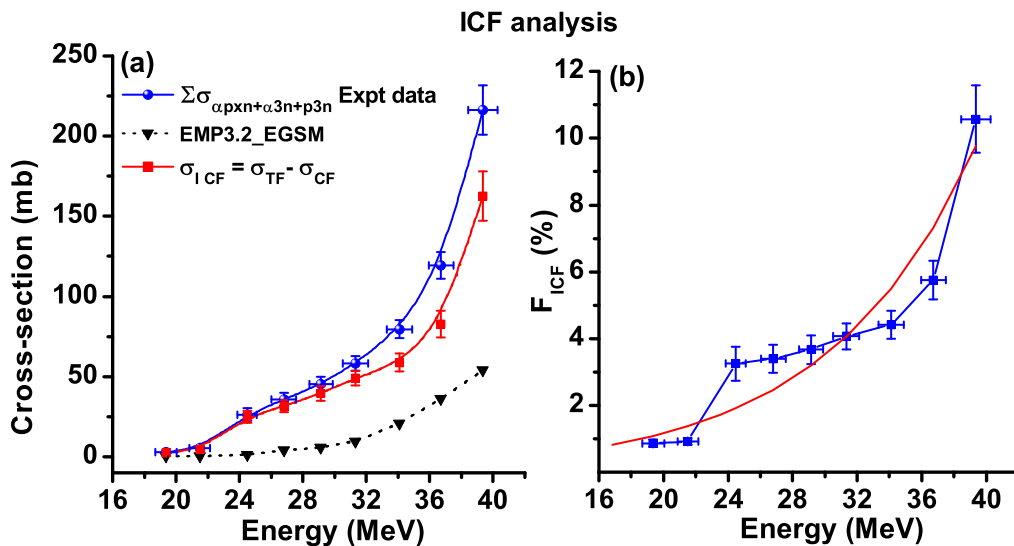


FIG. 6. (a) Variation of CF and ICF cross sections, and (b) variation of ICF strength fraction with projectile energy for $^7\text{Li} + ^{89}\text{Y}$ reaction. Fitted line is to guide the eye.

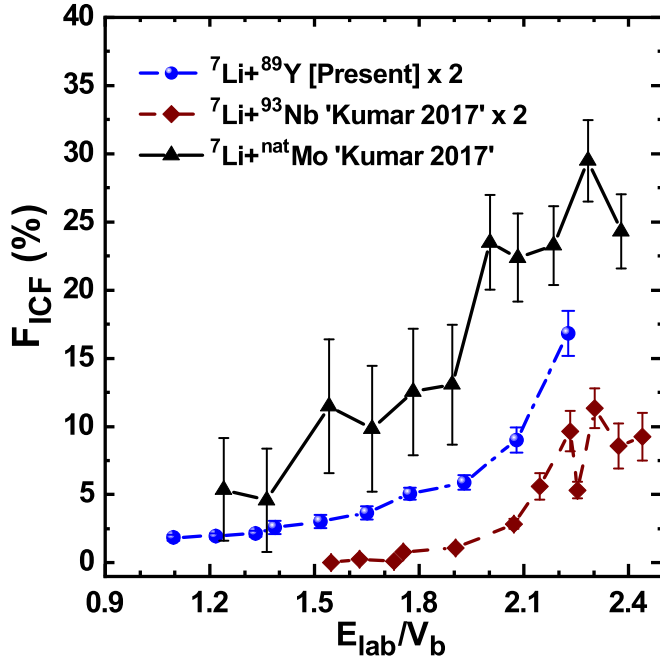
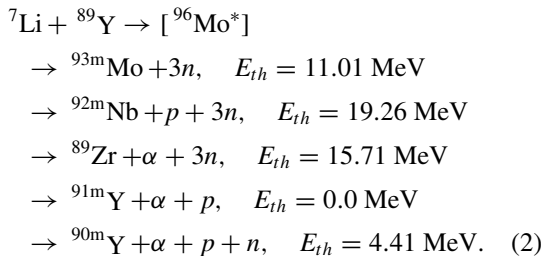


FIG. 7. ICF strength fraction (%) as a function of reduced projectile energy (E_{lab}/V_b) for ${}^7\text{Li} + {}^{89}\text{Y}$, ${}^7\text{Li} + {}^{93}\text{Nb}$; “Kumar 2017” [9] and ${}^7\text{Li} + {}^{\text{nat}}\text{Mo}$; “Kumar 2017” [6] systems, where V_b represents the Coulomb barrier in the laboratory equivalent.

of ${}^{91m,90m}\text{Y}$, ${}^{92m}\text{Nb}$, and ${}^{89}\text{Zr}$ could be due to the interplay of CF and ICF processes.

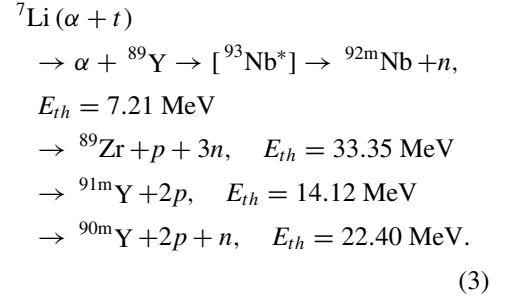
CF: Complete fusion of ${}^7\text{Li}$ in ${}^{89}\text{Y}$ leads to the formation of a compound nucleus ${}^{96}\text{Mo}^*$ in the excited state which may decay through the emission of light particles (e.g., p , n , α) and produce residual nuclei [Eq. (2)]:



ICF: ${}^7\text{Li}$ may break up into its constituent fragments ($\alpha + t$), and one of the fragments fuses with the target nucleus, forming a reduced CN, and remaining one fly away in the forward direction as a spectator. The following ICF processes could be responsible for the vast production of ${}^{92m}\text{Nb}$, ${}^{89}\text{Zr}$, ${}^{91m}\text{Y}$, and ${}^{90m}\text{Y}$ in the ${}^7\text{Li} + {}^{89}\text{Y}$ reaction. A quantitative analysis of the ICF is discussed in the next section.

(a) The fusion of an α particle, a direct breakup component of ${}^7\text{Li}$, in ${}^{89}\text{Y}$ leads to the formation of ${}^{93}\text{Nb}$ in the excited state, which may emit neutrons and protons to form ${}^{92m}\text{Nb}$, ${}^{89}\text{Zr}$, ${}^{90m}\text{Y}$, and ${}^{91m}\text{Y}$ [Eq. (3)], and t moves with the proportionate velocity as a spectator. Similarly,

fusion of t in ${}^{89}\text{Y}$ may result in the production of ${}^{89}\text{Zr}$, ${}^{90m}\text{Y}$, and ${}^{91m}\text{Y}$ via the $3n$, pn , and p channel, respectively:



However, the possibility of ${}^{89}\text{Zr}$ production through the fusion of an α particle in ${}^{89}\text{Y}$ is unlikely due to its high reaction threshold of 33.35 MeV.

(b) One-neutron stripping from ${}^7\text{Li}$ in the nuclear field leads to the formation of ${}^{90}\text{Y}$ (or ${}^{90m}\text{Y}$), and ${}^6\text{Li}$ may dissociate into $\alpha + d$; fusion of one of the breakup components (α or d) with the target nuclei ${}^{89}\text{Y}$ or ${}^{90}\text{Y}$ may yield the production of ${}^{92m}\text{Nb}$, ${}^{89}\text{Zr}$, ${}^{91m}\text{Y}$, and ${}^{90m}\text{Y}$ through the emission of light particles, and the other component moves in the forward direction as spectator.

However, the production of ${}^{89}\text{Zr}$ through the ${}^{90}\text{Y}(d, 3n){}^{89}\text{Zr}$ reaction is favorable as compared with ${}^{90}\text{Y}(\alpha, p4n){}^{89}\text{Zr}$ reaction due to its large threshold energy.

(c) One-proton pickup by ${}^7\text{Li}$ from the target forms an unstable ${}^8\text{Be}$, which possibly breaks up into $\alpha + \alpha$, and ${}^{88}\text{Sr}$. If any one of the α particles fuses with ${}^{89}\text{Y}$, it would lead to the production of ${}^{92m}\text{Nb}$, ${}^{89}\text{Zr}$, ${}^{90m}\text{Y}$, and ${}^{91m}\text{Y}$ following Eq. (3). Similarly, the fusion of an α particle in ${}^{88}\text{Sr}$ could produce ${}^{89}\text{Zr}$, ${}^{91m}\text{Y}$, and ${}^{90m}\text{Y}$, while the remaining α particle moves in the forward direction with its initial velocity. The optimum Q value for the one-proton pickup by ${}^7\text{Li}$ is comparable with the ground-state Q value within the incident energy range.

Although several favorable routes that include both CF and ICF processes could contribute to the production of ${}^{91m}\text{Y}$ and ${}^{90m}\text{Y}$, a direct fusion of ${}^7\text{Li}$, and the fusion of ICF fragments (α or t) in ${}^{89}\text{Y}$ are more likely. Neutron stripping from the ${}^7\text{Li}$ to the ${}^{89}\text{Y}$ is also another appealing route of formation of ${}^{90m}\text{Y}$.

The total residual cross section ($\sum \sigma_{\text{res}}$) from the ${}^7\text{Li} + {}^{89}\text{Y}$ reaction at various projectile energies, and the measured residues are listed in Table II.

B. Analysis of incomplete fusion

An analysis of the observed enhancement in cross sections of the residues, ${}^{92m}\text{Nb}$, ${}^{89}\text{Zr}$, ${}^{90m}\text{Y}$, and ${}^{91m}\text{Y}$ has been carried out to understand the contribution of ICF processes by comparing them with the theoretical model calculations from

EMPIRE up to 40 MeV energy. Since EMPIRE does not consider the break-up or ICF mechanism in its calculation, the production cross sections of the residues are purely from the complete fusion of ${}^7\text{Li}$ in ${}^{89}\text{Y}$. It has been observed that the cross sections of ${}^{93m}\text{Mo}$, produced through the $3n$ channel, is well described by EMPIRE with the EGSM level density, while the deployment of the same set of input parameters in EMPIRE largely underpredicts the residual cross sections of ${}^{92m}\text{Nb}$, ${}^{89}\text{Zr}$, ${}^{90m}\text{Y}$, and ${}^{91m}\text{Y}$. Thus, the observed enhancement in the measured cross sections is attributed to the ICF reactions, and the ICF strength has been analyzed with the help of the data-reduction method [6,8,27].

The total cross section of the ICF processes (σ_{ICF}) is calculated from the α - and p -emitting channels by using the relation

$$\sum \sigma_{ICF} = \sigma_{TF}^{\sum \alpha 3n + \alpha p + \alpha pn + p 3n} - \sigma_{CF}^{\sum \alpha 3n + \alpha p + \alpha pn + p 3n},$$

where σ_{TF} and σ_{CF} are the sum of experimental cross sections and theoretical cross sections estimated from EMPIRE, respectively. A comparison has been made between the sum of measured cross sections (blue line) from $\alpha 3n$, αp , αpn , and $p 3n$ channels (σ_{TF}), the theoretical predictions (black line) from EMPIRE for those channels (σ_{CF}), and the ICF cross sections (red line; σ_{ICF}), depicted in Fig. 6(a). It is worth mentioning that the relative separation between the TF and CF cross sections increases with increasing projectile energy [Fig. 6(a)], it signifies that the breakup probability of the weakly bound ${}^7\text{Li}$ projectile increases with increasing energy; a similar trend was observed in Refs. [6,8].

To quantify the contribution of ICF over CF, ICF strength fraction ($F_{ICF}\%$) has been defined as $F_{ICF} = (\sigma_{ICF}/\sigma_{TF}^{\text{theor}}) \times 100\%$, where $\sigma_{TF}^{\text{theor}}$ is the total theoretical fusion (sum of all residues) cross section predicted by EMPIRE. The variation of F_{ICF} has been shown in Fig. 6(b), which shows an increasing trend of F_{ICF} with respect to the increasing projectile energy. F_{ICF} varies between $\approx 1\%$ – 11% within the experimental energy range, 19–40 MeV, resulting in an average F_{ICF} contribution of $\approx 3\%$ per channel. The line fit through the data in Fig. 6(b) is to guide the eye.

Figure 7 depicts the variation of F_{ICF} for the α channels as a function of reduced energy (E_{lab}/V_b) from the ${}^7\text{Li}$ induced reactions in ${}^{89}\text{Y}$, ${}^{93}\text{Nb}$, and ${}^{\text{nat}}\text{Mo}$ [6,9]. Although ICF fraction shows an increasing trend for all the systems, yet it is relatively higher for ${}^7\text{Li} + {}^{\text{nat}}\text{Mo}$ reaction as compared with ${}^7\text{Li} + {}^{89}\text{Y}$ and ${}^7\text{Li} + {}^{93}\text{Nb}$. It is worth mentioning that Kumar *et al.* [6,9] considered five αxn and one αxn channel for the ${}^7\text{Li} + {}^{\text{nat}}\text{Mo}$ and ${}^7\text{Li} + {}^{93}\text{Nb}$ reactions, respectively, while we could include three α channels for the ${}^7\text{Li} + {}^{89}\text{Y}$ reaction to calculate the contribution of ICF strength fractions.

C. Nuclear potential parameters

Determination of nuclear potential parameters such as the barrier height between the interacting nuclei and barrier radius from the experiment is important to follow the nature of heavy-ion reactions. However, it is hard to extract the fusion barrier from direct methods; therefore, it is indirectly obtained from the measured fusion cross section (sum of the residual cross sections) data. The theoretical models which are based on the 1D-BPM can predict the fusion cross sections. For low-energy light-ion reactions in the intermediate-mass region, the contribution of direct processes remain negligibly small; hence $\sigma_{\text{fus}} \approx \sigma_r$. Therefore, the fusion cross section σ_{fus} can be expressed as

$$\sigma_{\text{fus}}(E_{c.m.}) = \pi \lambda^2 \sum_{l=0}^{\infty} (2l+1) T_l(E_{c.m.}). \quad (4)$$

The probability for the absorption of the l th partial wave $T_l(E_{c.m.}) = [1 + \exp\{(2\pi/\hbar\omega_l)(V_{bl} - E_{c.m.})\}]^{-1}$ can be obtained by using Hill-Wheeler approach; V_{bl} is the barrier height in MeV corresponding to angular momentum l , ω_l is the vibrational frequency of the harmonic oscillator in the parabolic potential, and $E_{c.m.}$ is the energy of the center-of-mass system. The parameter ω_l and the effective interaction potential V_l is related by

$$\hbar\omega_l = \left[\frac{\hbar^2}{\mu} \frac{d^2 V_l}{dr^2} \right]^{1/2},$$

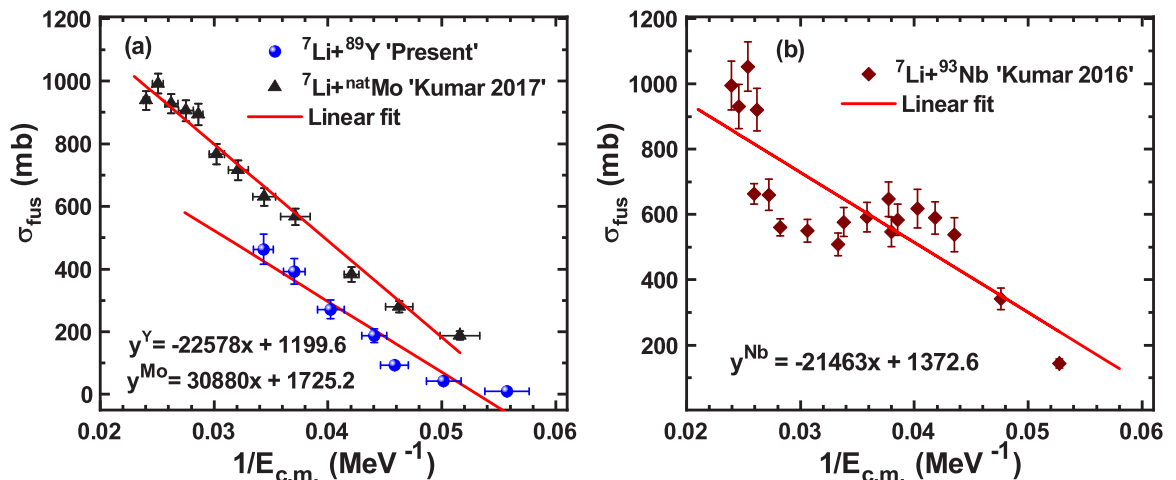


FIG. 8. Variation of total fusion cross sections σ_{fus} as a function of energy ($1/E_{c.m.}$) for (a) ${}^7\text{Li} + {}^{89}\text{Y}$ (blue circles) and ${}^7\text{Li} + {}^{\text{nat}}\text{Mo}$; Kumar 2017 (black triangles) [6], and (b) ${}^7\text{Li} + {}^{93}\text{Nb}$; Kumar 2016 (wine color) [7] reactions. Solid lines are linear fits through the data.

where μ , R_l are the reduced mass and the radial separation of the colliding partners for l th partial wave. Similarly, $\hbar\omega_l$ is referred to as the barrier curvature of the fusion barrier for the l th partial wave. If the curvature and barrier radius R_{bl} are independent of angular momentum ($l = 0$) then they can be approximated as the S -wave values $\hbar\omega_l = \hbar\omega$ and $R_{bl} = R_b$, hence the extraction of the fusion barrier can be done from a fitting of the measured fusion cross section with Wong's formula [59] [Eq. (5)]:

$$\sigma_{\text{fus}}(E_{\text{c.m.}}) = \frac{R_b^2 \hbar\omega}{2E_{\text{c.m.}}} \ln \left\{ 1 + \exp \left[\frac{2\pi}{\hbar\omega} (E_{\text{c.m.}} - V_b) \right] \right\}, \quad (5)$$

where V_b , R_b , and $\hbar\omega$ are the barrier height, barrier radius, and barrier curvature, respectively. For the energies well above the Coulomb barrier, i.e., $E_{\text{c.m.}} - V_b \geq \hbar\omega/2\pi$, Eq. (5) leads to the simplified classical fusion cross section

$$\sigma_{\text{fus}}(E_{\text{c.m.}}) = \pi R_b^2 \left(1 - \frac{V_b}{E_{\text{c.m.}}} \right), \quad (6)$$

which shows a linear dependence of σ_{fus} on $1/E_{\text{c.m.}}$ above barrier energies. The total residual cross sections σ_{fus} measured from the ${}^7\text{Li} + {}^{89}\text{Y}$ reaction are linear in inverse incident energy, as shown in Fig. 8(a). Three higher-energy points have been omitted here to obtain the best linear fit through the measured data to estimate the Coulomb barrier, because it is known that Wong's formula quickly deviates from reality for light systems as the energy increases [60]. The estimated barrier height and radius from the measured cross sections are 18.82 MeV and 6.18 fm, respectively, whereas the predicted barrier height from the Bass model is 16.38 MeV, which is close to our measurement. The calculated barrier radius from $R_b = 1.2(A_p^{1/3} + A_T^{1/3})$ is 7.65 fm, where A_p and A_T are mass numbers of projectile and target, respectively.

A similar trend in the measured σ_{fus} has also been observed for ${}^7\text{Li} + {}^{93}\text{Nb}$ [7] and ${}^7\text{Li} + {}^{\text{nat}}\text{Mo}$ [6] with respect to $1/E_{\text{c.m.}}$, as depicted in Figs. 8(a) and 8(b), respectively. From the linear fit of the data, the values of V_b and R_b have been calculated for the ${}^7\text{Li} + {}^{93}\text{Nb}$ [7] and ${}^7\text{Li} + {}^{\text{nat}}\text{Mo}$ [6] systems in the similar mass range to compare with those obtained from the ${}^7\text{Li} + {}^{89}\text{Y}$ system, and are tabulated in Table III. Although a good agreement has been observed between the experimental and theoretical values, the measured V_b is slightly high for ${}^7\text{Li} + {}^{89}\text{Y}$ and slightly low for ${}^7\text{Li} + {}^{93}\text{Nb}$ compared with the expected barrier heights.

D. Application of ${}^{93m}\text{Mo}$

Due to its moderate half-life of 6.85 h and high-intensity γ lines of 263.05 keV (57.4%), 684.69 keV (99.9%), and 1477.14 keV (99.1%), ${}^{93m}\text{Mo}$ among other radioisotopes of molybdenum has the potential to be used in radiopharmaceuti-

TABLE III. Nuclear potential parameters for various ${}^7\text{Li}$ -induced reactions.

Reaction	V_b [MeV] (Expt.)	R_b [fm] (Expt.)	V_b [MeV] (Calc.)	R_b [fm] (Calc.)
${}^7\text{Li} + {}^{89}\text{Y}$	18.82	6.18	16.38	7.65
${}^7\text{Li} + {}^{93}\text{Nb}$ [7]	16.14	6.88	17.12	7.73
${}^7\text{Li} + {}^{\text{nat}}\text{Mo}$ [6]	17.90	7.41	17.45	7.78

cal science, diagnostic imaging, or for therapeutic purposes. The maximum production cross section of 396.8 ± 38.6 mb at 31.3 MeV energy has been measured for ${}^{93m}\text{Mo}$, which could produce ≈ 374 MBq/C activity at a 3 mg/cm² target. Since the production cross sections of other radionuclides (${}^{92m}\text{Nb}$, ${}^{89}\text{Zr}$, ${}^{90m}\text{Y}$, and ${}^{91m}\text{Y}$) at this energy and below are significantly low, minimal undesired activity is expected to be present in the thick-target yield of ${}^{93m}\text{Mo}$. However, pure ${}^{93m}\text{Mo}$ could be obtained from the ${}^{89}\text{Y}$ matrix by employing a suitable chemical separation technique.

V. CONCLUSION

This paper reports the first measurement of the residual cross sections of ${}^{93m}\text{Mo}$, ${}^{92m}\text{Nb}$, ${}^{89}\text{Zr}$, ${}^{90m}\text{Y}$, and ${}^{91m}\text{Y}$ from the ${}^7\text{Li} + {}^{89}\text{Y}$ reaction up to 40 MeV incident energy. The cross-section data have been analyzed by using the framework of the theoretical EQ and PEQ models. It shows that the mixing of EQ and PEQ models is the key to reproduce the cross sections of ${}^{93m}\text{Mo}$ produced in the $3n$ channel, indicating the role of the CF process. It is speculated that the ICF processes plays a substantial role in the production of ${}^{92m}\text{Nb}$, ${}^{89}\text{Zr}$, ${}^{90m}\text{Y}$, and ${}^{91m}\text{Y}$ residues, which are also expected to be produced through the p - and α -emitting channels after the complete fusion of ${}^7\text{Li}$ in ${}^{89}\text{Y}$. The ICF strength fraction has an increasing trend with increasing projectile energy. Nuclear potential parameters are estimated from the measured data and are in good agreement with the theoretical parameters estimated from the Bass model. The cross-section data over a wide energy range might be useful for the optimized production of ${}^{93m}\text{Mo}$ for applications.

ACKNOWLEDGMENTS

The authors profoundly thank the BARC-TIFR Pelletron team for their assistance during the experiment and colleagues from the laboratory for their ardent teamwork during the experiment. We thank Dr. M. Blann for the useful discussion on the model calculation. A research grant from SERB (IN), CRG/2018/002354, and the fellowship from MHRD, Government of India, are also gratefully acknowledged.

- [1] A. M. Stefanini, L. Corradi, A. M. Vinodkumar, Y. Feng, F. Scarlassara, G. Montagnoli, S. Beghini, and M. Bisogno, *Phys. Rev. C* **62**, 014601 (2000).
 [2] S. Kalkal, S. Mandal, N. Madhavan, E. Prasad, S. Verma, A. Jhingam, R. Sandal, S. Nath, J. Gehlot, B. R. Behera, M.

- Saxena, S. Goyal, D. Siwal, R. Garg, U. D. Pramanik, S. Kumar, T. Varughese, K. S. Golda, S. Muralithar, A. K. Sinha, and R. Singh, *Phys. Rev. C* **81**, 044610 (2010).
 [3] R. G. Stokstad, Y. Eisen, S. Kaplanis, D. Pelte, U. Smilansky, and I. Tseruya, *Phys. Rev. Lett.* **41**, 465 (1978).

- [4] J. D. Bierman, P. Chan, J. F. Liang, M. P. Kelly, A. A. Sonzogni, and R. Vandenbosch, *Phys. Rev. Lett.* **76**, 1587 (1996).
- [5] A. M. Stefanini, G. Fortuna, A. Tivelli, W. Meczynski, S. Beghini, C. Signorini, S. Lunardi, and M. Morando, *Phys. Rev. C* **30**, 0888 (1984).
- [6] D. Kumar, M. Maiti, and S. Lahiri, *Phys. Rev. C* **96**, 014617 (2017).
- [7] D. Kumar, M. Maiti, and S. Lahiri, *Phys. Rev. C* **94**, 044603 (2016).
- [8] P. P. Singh, B. P. Singh, M. K. Sharma, Unnati, D. P. Singh, R. Prasad, R. Kumar, and K. S. Golda, *Phys. Rev. C* **77**, 014607 (2008).
- [9] D. Kumar and M. Maiti, *Phys. Rev. C* **96**, 044624 (2017).
- [10] L. R. Gasques, D. J. Hinde, M. Dasgupta, A. Mukherjee, and R. G. Thomas, *Phys. Rev. C* **79**, 034605 (2009).
- [11] M. Shuaib, V. R. Sharma, A. Yadav, P. P. Singh, M. K. Sharma, D. P. Singh, R. Kumar, R. P. Singh, S. Muralithar, B. P. Singh, and R. Prasad, *Phys. Rev. C* **94**, 014613 (2016).
- [12] P. R. S. Gomes, R. Linares, J. Lubian, C. C. Lopes, E. N. Cardozo, B. H. F. Pereira, and I. Padron, *Phys. Rev. C* **84**, 014615 (2011).
- [13] R. Rafiei, R. du Rietz, D. H. Luong, D. J. Hinde, M. Dasgupta, M. Evers, and A. Diaz-Torres, *Phys. Rev. C* **81**, 024601 (2010).
- [14] A. Chauhan and M. Maiti, *Phys. Rev. C* **99**, 034608 (2019).
- [15] K. Siwek-Wilczynska, E. H. du Marchievan Voorthuysen, J. van Popta, R. H. Siemssen, and J. Wilczyński, *Phys. Rev. Lett.* **42**, 1599 (1979).
- [16] J. Wilczynski, K. Siwek-Wilczynska, J. V. Driel, S. Gonggrijp, D. C. J. M. Hageman, R. V. F. Janssens, J. Lukasiak, R. H. Siemssen, and S. Y. V. D. Werf, *Nucl. Phys. A* **373**, 109 (1982).
- [17] L. F. Canto, P. R. S. Gomes, R. Donangelo, J. Lubian, and M. S. Hussein, *Phys. Rep.* **596**, 1 (2015).
- [18] L. F. Canto, P. R. S. Gomes, R. Donangelo, and M. S. Hussein, *Phys. Rep.* **424**, 1 (2006).
- [19] I. Padron, P. R. S. Gomes, R. M. Anjos, J. Lubian, C. Muri, J. J. S. Alves, G. V. Martí, M. Ramírez, A. J. Pacheco, O. A. Capurro, J. O. F. Niello, J. E. Testoni, D. Abriola, and M. R. Spinella, *Phys. Rev. C* **66**, 044608 (2002).
- [20] R. M. Anjos, C. Muri, J. Lubian, P. R. S. Gomes, I. Padron, J. J. S. Alves, G. V. Martí, J. O. F. Niello, A. J. Pacheco, O. A. Capurro, D. Abriola, J. E. Testoni, M. Ramírez, R. Liguori Neto, and N. Added, *Phys. Lett. B* **534**, 45 (2002).
- [21] H. Kumawat, V. Jha, V. V. Parkar, B. J. Roy, S. K. Pandit, R. Palit, P. K. Rath, C. S. Palshetkar, S. K. Sharma, S. Thakur, A. K. Mohanty, A. Chatterjee, and S. Kailas, *Phys. Rev. C* **86**, 024607 (2012).
- [22] S. P. Hu, G. L. Zhang, J. C. Yang, H. Q. Zhang, P. R. S. Gomes, J. Lubian, X. G. Wu, J. Zhong, C. Y. He, Y. Zheng, C. B. Li, G. S. Li, W. W. Qu, F. Wang, L. Zheng, L. Yu, Q. M. Chen, P. W. Luo, H. W. Li, Y. H. Wu, W. K. Zhou, B. J. Zhu, and H. B. Sun, *Phys. Rev. C* **91**, 044619 (2015).
- [23] P. K. Rath, S. Santra, N. L. Singh, R. Tripathi, V. V. Parkar, B. K. Nayak, K. Mahata, R. Palit, S. Kumar, S. Mukherjee, S. Appannababu, and R. K. Choudhury, *Phys. Rev. C* **79**, 051601(R) (2009).
- [24] P. K. Rath, S. Santra, N. L. Singh, B. K. Nayak, K. Mahata, R. Palit, K. Ramachandran, S. K. Pandit, A. Parihari, A. Pal, S. Appannababu, S. K. Sharma, D. Patel, and S. Kailas, *Phys. Rev. C* **88**, 044617 (2013).
- [25] A. Mukherjee, S. Roy, M. K. Pradhan, M. S. Sarkar, P. Basua, B. Dasmahapatra, T. Bhattacharya, S. Bhattacharya, S. K. Basu, A. Chatterjee, V. Tripathi, and S. Kailas, *Phys. Lett. B* **636**, 91 (2006).
- [26] C. S. Palshetkar, S. Santra, A. Chatterjee, K. Ramachandran, S. Thakur, S. K. Pandit, K. Mahata, A. Shrivastava, V. V. Parkar, and V. Nanal, *Phys. Rev. C* **82**, 044608 (2010).
- [27] P. R. S. Gomes, I. Padron, E. Crema, O. A. Capurro, J. O. Fernández Niello, A. Arazi, G. V. Martí, J. Lubian, M. Trotta, A. J. Pacheco, J. E. Testoni, M. D. Rodríguez, M. E. Ortega, L. C. Chamon, R. M. Anjos, R. Veiga, M. Dasgupta, D. J. Hinde, and K. Hagino, *Phys. Rev. C* **73**, 064606 (2006).
- [28] M. Dasgupta, P. R. S. Gomes, D. J. Hinde, S. B. Moraes, R. M. Anjos, A. C. Berriman, R. D. Butt, N. Carlin, J. Lubian, C. R. Morton, J. O. Newton, and A. Szanto de Toledo, *Phys. Rev. C* **70**, 024606 (2004).
- [29] O. A. Capurro, A. J. Pacheco, A. Arazi, P. F. F. Carnelli, J. O. F. Niello, and D. M. Heimann, *Nucl. Phys. A* **945**, 186 (2016).
- [30] S. K. Pandit, A. Shrivastava, K. Mahata, N. Keeley, V. V. Parkar, P. C. Rout, K. Ramachandran, I. Martel, C. S. Palshetkar, A. Kumar, A. Chatterjee, and S. Kailas, *Phys. Rev. C* **93**, 061602(R) (2016).
- [31] A. Shrivastava, A. Navin, N. Keeley, K. Mahata, K. Ramachandran, V. Nanal, V. V. Parkar, A. Chatterjee, and S. Kailas, *Phys. Lett. B* **633**, 463 (2006).
- [32] M. Gull, K. Kumar, S. Ali, T. Ahmad, S. Dutt, I. A. Rizvi, A. Agarwal, and R. Kumar, *Phys. Rev. C* **98**, 034603 (2018).
- [33] A. Chauhan, M. Maiti, and S. Lahiri, *Phys. Rev. C* **99**, 064609 (2019).
- [34] D. Kumar and M. Maiti, *Phys. Rev. C* **95**, 064602 (2017).
- [35] M. Maiti and S. Lahiri, *Phys. Rev. C* **84**, 067601 (2011).
- [36] M. Maiti, *Phys. Rev. C* **84**, 044615 (2011).
- [37] M. Maiti and S. Lahiri, *Phys. Rev. C* **81**, 024603 (2010).
- [38] D. Kumar, M. Maiti, and S. Lahiri, *Sep. Sci. Technol. (Philadelphia, PA, U. S.)* **52**, 2372 (2017).
- [39] M. Maiti and S. Lahiri, *Radiochim. Acta* **99**, 359 (2011).
- [40] M. Maiti and S. Lahiri, *Radiochim. Acta* **103**, 7 (2015).
- [41] M. Maiti, *Radiochim. Acta* **101**, 437 (2013).
- [42] M. Maiti and S. Lahiri, *Phys. Rev. C* **79**, 024611 (2009).
- [43] M. Maiti, *J. Radioanal. Nucl. Chem.* **297**, 319 (2013).
- [44] M. Maiti and S. Lahiri, *Radiochim. Acta* **97**, 663 (2009).
- [45] M. Maiti and S. Lahiri, *J. Radioanal. Nucl. Chem.* **281**, 501 (2009).
- [46] M. K. Sharma, P. P. Singh, D. P. Singh, A. Yadav, V. R. Sharma, I. Bala, R. Kumar, Unnati, B. P. Singh, and R. Prasad, *Phys. Rev. C* **91**, 014603 (2015).
- [47] J. F. Ziegler, M. D. Ziegler, and J. P. Biersack, *Nucl. Instrum. Methods Phys. Res., Sect. B* **268**, 1818 (2010).
- [48] B. Wilken and T. A. Fritz, *Nucl. Instrum. Methods* **138**, 331 (1976).
- [49] J. Kemmer and R. Hofmann, *Nucl. Instrum. Methods* **176**, 543 (1980).
- [50] M. Blann, *Phys. Rev. C* **54**, 1341 (1996).
- [51] M. Herman, R. Capote, B. V. Carlson, P. Obložinský, M. Sin, A. Trkov, H. Wienke, and V. Zerkin, *Nucl. Data Sheets* **108**, 2655 (2007).
- [52] C. H. Dasso and S. Landowne, *Comput. Phys. Commun.* **46**, 187 (1987).
- [53] A. Gilbert and A. G. W. Cameron, *Can. J. Phys.* **43**, 1446 (1965).
- [54] A. V. Ignatyuk, J. L. Weil, S. Raman, and S. Kahane, *Phys. Rev. C* **47**, 1504 (1993).

- [55] A. D'Arrigo, G. Giardina, M. Herman, A. V. Ignatyuk, and A. Taccone, *J. Phys. G* **20**, 365 (1994).
- [56] D. Chattopadhyay, S. Santra, A. Pal, A. Kundu, K. Ramachandran, R. Tripathi, B. J. Roy, T. N. Nag, Y. Sawant, B. K. Nayak, A. Saxena, and S. Kailas, *Phys. Rev. C* **97**, 051601(R) (2018).
- [57] S. Santra, S. Kailas, V. V. Parkar, K. Ramachandran, V. Jha, A. Chatterjee, P. K. Rath, and A. Parihari, *Phys. Rev. C* **85**, 014612 (2012).
- [58] S. K. Pandit, A. Shrivastava, K. Mahata, V. V. Parkar, N. Keeley, P. C. Rout, K. Ramachandran, C. S. Palshetkar, I. Martel, A. Kumar, A. Chatterjee, and S. Kailas, *Phys. Rev. C* **100**, 014618 (2019).
- [59] C. Y. Wong, *Phys. Rev. Lett.* **31**, 766 (1973).
- [60] N. W. Lwin, N. N. Htike, and K. Hagino, *Phys. Rev. C* **95**, 064601 (2017).
- [61] National Nuclear Data Center, Brookhaven National Laboratory, <http://www.nndc.bnl.gov/nudat2/>.